Supplementary material: High-pressure crystal structure and phase transitions in B_2O_3

Dominik Spahr*[,a], Sean S. Sebastian[b], Lukas Brüning[b], Pascal L. Jurzick[b], Ninel Sharapova[a], Lkhamsuren Bayarjargal[a], Elena Bykova[a], Maxim Bykov[b], Victor Milman[c], Björn Winkler[a]

[a]*Goethe University Frankfurt, Institute of Geosciences, Altenhöferallee 1, 60438 Frankfurt, Germany*
[b]*Goethe University Frankfurt, Institute of Inorganic and Analytical Chemistry, Max-von-Laue-Straße 7, 60438 Frankfurt, Germany*
[c]*Dassault Systèmes BIOVIA, 334 Cambridge Science Park, Cambridge CB4 0WN, United Kingdom*

1. Methods

1.1. Sample material

The high-pressure experiments were carried out using commercial boron trioxide (B_2O_3) powder (99.999% purity, Merck KGaA, Darmstadt, Germany) as starting material. The B_2O_3 powder was dried at ≈ 580 K in a drying oven for 24 h prior the loading of the DAC and used as received without further purification. The CO_2 gas for the gas-jet was used as purchased (Nippon gases, purity ≥ 99.996%).

1.2. High-pressure experiments

The high-pressure experiment was carried out in similar manner to the synthesis of the hydrous borocarbonate B[μ-H$(CO_3)_2$] in a Boehler-Almax type diamond anvil cell (DAC).[1,2] The DAC was equipped with diamonds having an opening angle of 70° and 300 µm sized culets on both sides. We used a Re-gasket, which was pre-indented to thicknesses of ≈ 40 µm. Afterwards, a sample chamber with ≈ 100 µm diameter was drilled into the Re-gasket using a custom-built laser set-up. The pressure during compression of the DAC was derived from the position of the high frequency edge of the diamond Raman band and we assume an error of at least 5% due to non-hydrostatic conditions in the DAC.[3] In addition, we expect that the pressure conditions in the DAC before laser heating are very likely non-hydrostatic as CO_2-III may sustain pressure gradients up to 0.2 GPa µm^{-1} at high pressures without heating.[4]

First, a B_2O_3 piece with dimensions of ≈ 40 × 40 × 20 µm^3 was placed on the culet of the bottom diamond. Attempting the synthesis of an anhydrous boron carbonate, CO_2 was employed as a pressure transmitting medium and precursor for the synthesis. For the cryogenic loading the DAC was placed on a liquid nitrogen cooled Cu-holder and cooled down using a custom-built cryogenic loading system (see Spahr *et al.*[5]). The DAC was cooled down to ≈ 120 K and CO_2-I (dry ice) was directly condensed into the sample chamber from the CO_2 gas jet. We used a small nozzle to align the CO_2 gas jet with 5 l min^{-1} directly on the gap between upper diamond and the gasket. We used argon (5 l min^{-1}) as a purge gas in order to avoid the co-precipitation of H_2O and the formation of B[μ-H$(CO_3)_2$] after laser heating.[1] During the loading process the precipitation of the CO_2 in the sample chamber was monitored using an optical microscope and equipped with a camera. After the sample chamber was completely covered with dry-ice, the enclosure was opened and the DAC was tightly closed. Finally, the sample in the DAC was compressed stepwise to 50(3) GPa.

1.3. Laser heating

The B_2O_3 in the CO_2 environment was laser-heated from both sides using a custom-built set-up equipped with a Coherent Diamond K-250 pulsed CO_2 laser (λ = 10600 nm).[6] The laser power was adjusted to achieve a coupling of the laser to the sample, using a laser power between 1–6 W. The maximum temperature achieved during the laser-heating was $T_{max} \leq 2500(300)$ K. The temperatures were determined by the two-color pyrometer method, employing Planck and Wien fits.[7] The heating time at 50(3) GPa was ≈ 30 minutes. It is well established that laser-heating in DACs always suffers from large temperature gradients and the actual temperature is strongly dependent on the coupling of the laser with the sample, especially at lower temperatures. We estimate an uncertainty of at least ±15% of the nominal temperature in the laser-heated region depending on the focus of the laser beam, based on typical 2D temperature-gradient determination experiments performed in DACs.[8]

1.4. Raman spectroscopy

Raman spectroscopy at high-pressures and after decompression of the DAC was performed using an Oxford Instruments WITec alpha 300R Raman imaging microscope. The Raman microscope was equipped with an Olympus SLMPan N 50× objective. The measurements were performed using the 532 nm laser. We employed the 1200 grooves mm^{-1} grating of the WITec UHTS 300S (VIS-NIR) spectrograph in combination with an Andor DR316B-LDC-DD CCD detector for the measurements. The laser power was 100 mW on the sample and the spot size of the Raman laser was ≈ 0.8 µm. We assume a depth resolution of ≈ 6 µm in the direction of the laser beam. Raman maps were measured on a grid with a step-size of 1 µm. The background of the Raman spectra was corrected using the software package Fityk.[9]

*d.spahr@kristall.uni-frankfurt.de

1.5. Single-crystal synchrotron X-ray diffraction

Single-crystal synchrotron X-ray diffraction at 50(3) GPa was carried out at the ESRF in Grenoble, France, at the Materials Science Beamline line ID11.[10] The beam size on the sample was 0.6×0.6 μm^2 and the diffraction data were collected using an Eiger2 X 4M CdTe detector. We used a wavelength of 0.2846 Å (43.6 keV) and a detector to sample distance of 183.2 mm. The DAC was rotated by $\pm 33^\circ$ around the vertical axis perpendicular to the beam while collecting frames in 0.5° steps with 2 s acquisition time per frame.

The detector to sample distance was calibrated using the powder diffraction pattern of a CeO_2 standard in conjunction with the software DIOPTAS.[11] The diffractometer/detector geometry for the analysis of the single-crystal diffraction data was calibrated using diffraction data collected from a silicon single-crystal at ambient pressure. After the data collection, the reflections were indexed and integrated employing CrysAlis^{PRO} (version 43.67a).[12] We used the Domain Auto Finder program (DAFi) to find possible single-crystal domains for the subsequent data reduction.[13] The structure solution and refinement were performed using the software package OLEX2 employing SHELXT for the crystal structure determination and SHELXL for the refinement.[14,15,16]

1.6. Density functional theory-based calculations

First-principles calculations were carried out within the framework of density functional theory (DFT), employing the Perdew-Burke-Ernzerhof (PBE) exchange-correlation functional and the plane wave/pseudopotential approach implemented in the CASTEP simulation package.[17,18,19] "On the fly" norm-conserving or ultrasoft pseudopotentials generated using the descriptors in the CASTEP data base were employed in conjunction with plane waves up to a kinetic energy cutoff of 1020 eV or 630 eV, for norm-conserving and ultrasoft pseudopotentials, respectively. The accuracy of the pseudopotentials is well established.[20] A correction scheme for van der Waals (v.d.W.) interactions was applied in the DFT-calculations. We employed the correction scheme developed by Tkatchenko and Scheffler.[21] A Monkhorst-Pack grid was used for Brillouin zone integrations.[22] We used a distance between grid points of <0.023 Å^{-1}. Convergence criteria for geometry optimization included an energy change of $<5 \times 10^{-6}$ eV atom^{-1} between steps, a maximal force of <0.008 eV Å^{-1} and a maximal component of the stress tensor <0.02 GPa. Phonon frequencies were obtained from density functional perturbation theory (DFPT) calculations.[23,24] Raman intensities were computed using DFPT with the "$2n + 1$" theorem approach.[25]

2. Results

2.1. Single-crystal synchrotron X-ray diffraction

In order to determine the structure of the unknown phase observed by Raman spectroscopy, we employed synchrotron X-ray diffraction. First, we collected X-ray diffraction data on a 2D grid across the sample chamber using a spot size of $\approx 0.6 \times 0.6$ µm^2 in order to locate promising positions for the collection of single-crystal diffraction data. In the second step, we performed synchrotron single-crystal X-ray diffraction on selected locations of the grid where unidentified reflections were present. Fig. S 1 a shows a part of the reciprocal space reconstruction for the ($hk\bar{1}$) plane of the single-crystal on which the crystal structure was determined, demonstrating the high quality of the collected diffraction data.

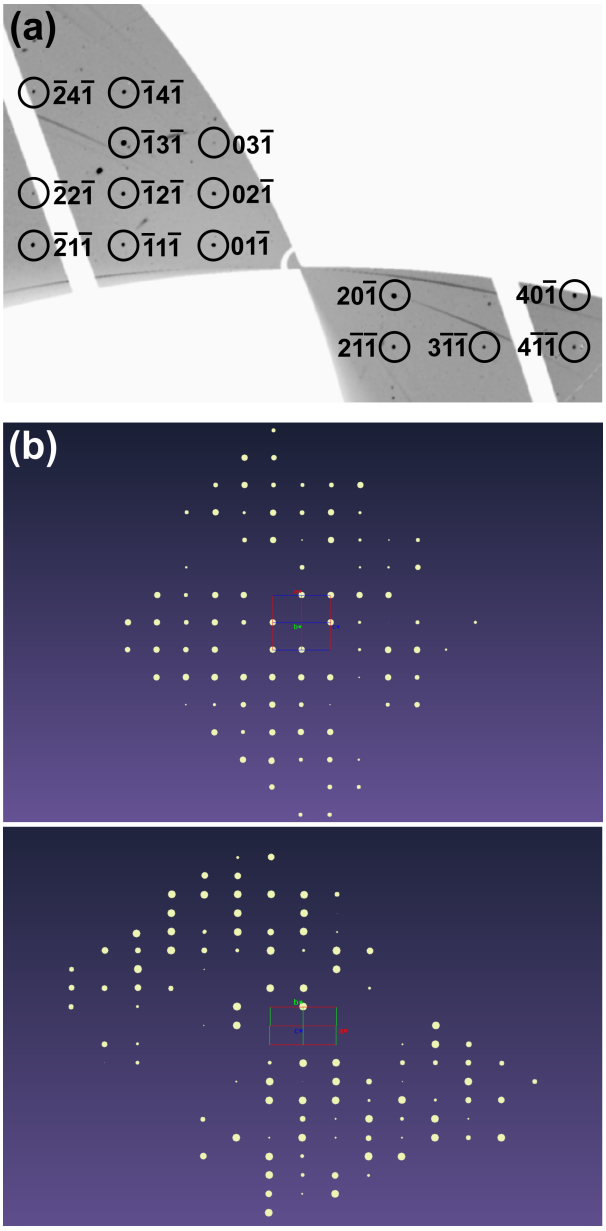

Figure S 1: (a) Reciprocal space reconstruction for the ($hk\bar{1}$) plane at 50(3) GPa. (b) Schematic depiction of the reflections in reciprocal space using the Ewald-Explorer in CrysAlis after data reduction which were later used for the refinement. Projections of the reciprocal space are shown along b^* (top) and c^* (bottom).

Besides the reflection of the unknown phase, we observed reflections and powder rings of CO_2-V, of B_2O_3-$Ccm2_1$ and of diamond in the collected diffraction data (Fig. S 1 a). Fig. S 1 b shows the projection of the reciprocal space along b^* (top) and c^* (bottom). The effect of the shading of diffracted beams due to the metallic body of the DAC and the effect of the inactive detector-areas due to the segments of the Eiger2 X detector can be observed.

The crystal structure of the unknown phase was solved from the single crystal diffraction data collected at 50(3) GPa in the orthorhombic space group $P2_12_12_1$ (No. 19) with $Z = 4$ and B_2O_3 composition (Table S 1). The low R_1-value of (3.7%) in combination with an acceptable reflection to parameter ratio (6.9:1) reveal a convincing structure refinement. The displacement parameters the boron and oxygen atoms were refined anisotropically. No constraints or restraints were applied for the refinement. The experimental crystallographic parameters at 50(3) GPa are in agreement with the data derived from the DFT calculations (Table S 1).

Table S 1: Structural parameters of the high-pressure polymorph B_2O_3-$P2_12_12_1$ at 50(3) GPa from single-crystal structure solution (ambient temperature) in comparison to data from DFT calculations at the same pressure (athermal limit).

	Single Crystal	**DFT**
Crystal data		
Crystal system	orthorhombic	orthorhombic
Space group	$P2_12_12_1$	$P2_12_12_1$
Chemical formula	B_2O_3	B_2O_3
M_r	69.62	69.62
a (Å)	4.1372(4)	4.1109
b (Å)	7.351(1)	7.2910
c (Å)	3.9417(6)	3.9241
α (°)	90.0	90.0
β (°)	90.0	99.0
γ (°)	90.0	90.0
V (Å^3)	119.88(3)	117.62
Z	4	4
Data collection		-
F_{000}	136	-
θ range (°)	2.26–15.48	-
measured reflections	445	-
independent reflections	317	-
reflections $I > 2\sigma(I)$	286	-
R_{int}	0.008	-
		-
Refinement		-
$R_1[I > 2\sigma(I)]$, $wR_2(I)$	0.037, 0.087	-
No. of reflections	317	-
No. of parameters	46	-
No. of restraints	0	-
No. of constraints	0	-
$\Delta\rho_{max}$, $\Delta\rho_{min}$ (e Å^{-3})	0.50, −0.45	-

Testing the experimental structural model of B_2O_3-$P2_12_12_1$ using the *PLATON*/checkCIF program does not suggests a higher space group symmetry or a centrosym-

metric crystal structure.[26] This is consistent with our DFT-based geometry optimization which retain the acentric space group symmetry and the crystal structure prediction by Dong *et al.*[27]. The atomic coordinates for B_2O_3-$P2_12_12_1$ are listed in Table S 2. The anisotropic displacement parameters of the boron and the oxygen atoms can be found in the cif-file.

Table S 2: Atomic coordinates and equivalent displacement parameters (Å^2) of B_2O_3-$P2_12_12_1$ at 50(3) GPa obtained by single crystal structure refinement.

Atom	Site	x	y	z	U^*_{eq}
B1	4*a*	0.4230(5)	0.5046(3)	0.5927(6)	0.0068(4)
B2	4*a*	0.5771(5)	0.6721(3)	0.1199(5)	0.0068(4)
O1	4*a*	0.4028(3)	0.5210(2)	0.9596(4)	0.0060(3)
O2	4*a*	0.5665(3)	0.6545(2)	0.4626(4)	0.0066(3)
O3	4*a*	0.9118(3)	0.6653(2)	0.0029(4)	0.0062(3)

* U_{eq} is derived as 1/3 of the orthogonalized U_{ij} tensor

2.2. *Compressibility of B_2O_3*

We used our DFT-based calculations to computed the p, V-relations for all three experimentally observed B_2O_3 polymorphs. In order to obtain the bulk modulus (K_0) and its pressure derivative (K_p) we fitted separate 3rd-order Birch-Murnaghan equation of states (EoS) to unit cell volumes obtained for the different polymorphs using the software package EOSFit7-GUI (Fig. S 2).[28,29,30] The theoretical bulk modulus of B_2O_3-$P2_12_12_1$ is $K_0 = 156(1)$ GPa with $K_p = 4.12(5)$, of B_2O_3-$Ccm2_1$ it is $K_0 = 146(6)$ GPa with $K_p = 3.6(2)$ and of B_2O_3-$P3_121$ it is $K_0 = 41.0(9)$ GPa with $K_p = 5.7(3)$.

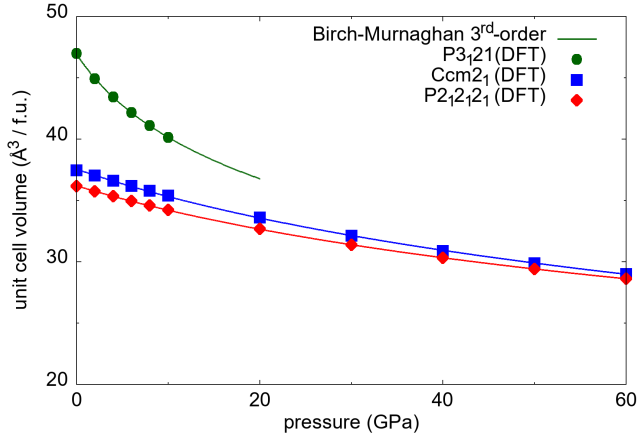

Figure S 2: 3rd-order Birch-Murnaghan EoS are fitted to the p, V-data of B_2O_3-$P3_121$ (0–10 GPa), B_2O_3-$Ccm2_1$ (0–60 GPa) and B_2O_3-$P2_12_12_1$ (0–60 GPa) obtained by DFT calculations.

2.3. *Elastic stiffness coefficients*

We computed the elastic stiffens coefficients (c_{ij}) for the three experimentally observed B_2O_3 polymorphs at 0 GPa using the stress strain-method (Table S 3).

Table S 3: Elastic stiffness coefficients (c_{ij}) for the three experimentally observed B_2O_3 polymorphs at 0 GPa obtained by DFT-based strain-stress calculations.

c_{ij}	$P3_121$ (GPa)	$Ccm2_1$ (GPa)	$P2_12_12_1$ (GPa)
c_{11}	159(1)	328.26(4)	400.3(8)
c_{22}	-	468(1)	338(2)
c_{33}	51(1)	480(2)	462(2)
c_{44}	47.3(3)	129.0(4)	176.6(2)
c_{55}	-	178.1(1)	121.9(6)
c_{66}	-	138.9(1)	158.9(7)
c_{12}	37.6(7)	42.4(7)	27(2)
c_{13}	10(1)	44(2)	44(1)
c_{14}	17.3(7)	-	-
c_{23}	-	45(2)	73(2)

The bulk moduli (K_0) derived from the DFT-based stress-strain calculations are in the same range than the values derived from the separate 3rd-order Birch-Murnaghan EoS fits to the p, V-data of the different polymorphs from the DFT-calculations: B_2O_3-$P3_121$ ($K_0 = 38.1(7)$ GPa), B_2O_3-$Ccm2_1$ ($K_0 = 166.0(5)$ GPa) and B_2O_3-$P2_12_12_1$ ($K_0 = 161.8(7)$ GPa). These results are consistent with the data reported by Dong *et al.*[27].

2.4. *Raman spectroscopy at ambient conditions*

We measured Raman spectroscopy during decompression of the DAC in order to understand if B_2O_3-$P2_12_12_1$ can be recovered at ambient conditions. The experimental Raman spectra show that the characteristic Raman modes of B_2O_3-$P2_12_12_1$ as well as of B_2O_3-$Ccm2_1$ are still present at ambient conditions after opening the DAC. Figure S 3 shows the experimental Raman data of B_2O_3-$P2_12_12_1$ and of B_2O_3-$Ccm2_1$ in comparison to the Raman spectra derived from our DFPT-calculations.

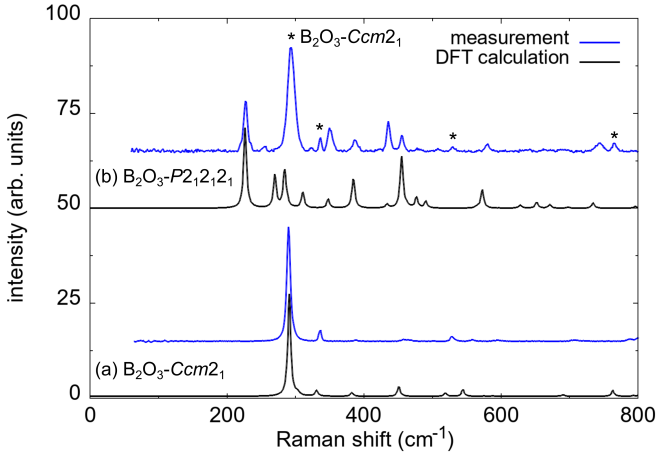

Figure S 3: Raman spectroscopy at ambient conditions after opening the DAC: (a) Raman spectra for B_2O_3-$Ccm2_1$. (b) Raman spectra for B_2O_3-$P2_12_12_1$. Experimental Raman spectra are shown in blue, DFT-based calculations are shown in black. The Raman shifts of the theoretical spectra were scaled by 1–3%. Peaks of B_2O_3-$Ccm2_1$ in the Raman spectrum of B_2O_3-$P2_12_12_1$ are marked by an asterisk (∗).

2.5. *Phonon dispersion curves*

We derived the phonon dispersion curves of B_2O_3-$P2_12_12_1$ at 50 GPa as well as at ambient pressure from our DFT-based calculations (Fig. S 4). The calculations show no negative frequencies for B_2O_3-$P2_12_12_1$ at 50 GPa and at ambient pressure and reveal that B_2O_3-$P2_12_12_1$ is dynamically stable at both pressure in the harmonic approximation and the athermal limit.

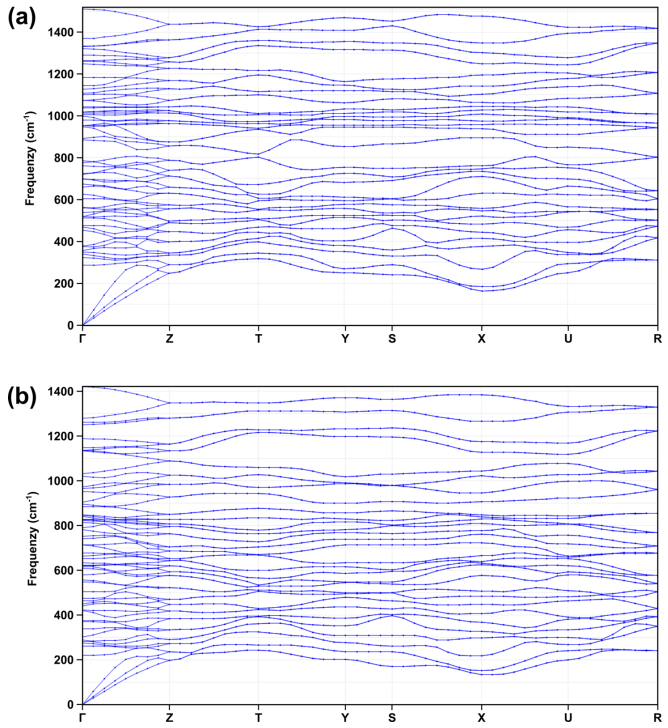

Figure S 4: Phonon dispersion curves for B_2O_3-$P2_12_12_1$ from DFT-based calculations: (a) at 50 GPa and (b) at ambient pressure.

2.6. *Crystal structure of B_2O_3-$P3_121$ (HP) at 20 GPa*

Our DFT-calculations suggest that another B_2O_3 polymorph ($P3_121$ with $Z = 3$) may be formed metastably at elevated pressures above $\approx$ 17 GPa. The lattice parameters at 20 GPa are $a = 4.0648$ Å and $c = 6.9180$ Å ($V = 98.99$ Å^3). The atomic coordinates for B_2O_3-$P3_121$ (HP) obtained by DFT-calculations are listed in Table S 4.

Table S 4: Atomic coordinates of B_2O_3-$P3_121$ (HP) at 20 GPa obtained by DFT-calculations.

Atom	**Site**	x	y	z
B1	6*c*	0.47090	0.30676	0.27140
O1	6*c*	0.60649	0.22567	0.08767
O2	3*a*	0.14266	0.00000	1/3

References

(1) Spahr, D.; Reuter, T. H.; Bykova, E.; Bayarjargal, L.; Brüning, L.; Kovalev, V.; Wedek, L.; Milman, V.; Wright, J.; Winkler, B. B[μ-H(CO_3)$_2$]: An Acentric Boron Hydrogencarbonate with [μ-H(CO_3)$_2$]$^{3-}$ Complex Anions. *Inorg. Chem.* **2025**, *64*, 19146–19150, DOI: 10.1021/acs.inorgchem.5c03153

(2) Boehler, R. New diamond cell for single–crystal X-ray diffraction. *Rev. Sci. Instrum.* **2006**, *77*, 115103, DOI: 10.1063/1.2372734

(3) Akahama, Y.; Kawamura, H.; Pressure calibration of diamond anvil Raman gauge to 310 GPa. *J. Appl. Phys.* **2006**, *100*, 043516, DOI: 10.1063/1.2335683

(4) Yoo, C. S.; Cynn, H.; Gygi, F.; Galli, G.; Iota, V.; Nicol, M.; Carlson, S.; Häusermann, D.; Mailhiot, C. Crystal Structure of Carbon Dioxide at High Pressure: "Superhard" Polymeric Carbon Dioxide. *Phys. Rev. Lett.* **1999**, *83*, 5527–5530, DOI: 10.1103/PhysRevLett.83.5527

(5) Spahr, D.; Bayarjargal, L.; Brüning, L.; Kovalev, V.; Bykova, E.; Bykov, M.; Milman, V.; Mezouar, M.; Winkler, B. Synthesis and Crystal Structure of Anhydrous Di-iodyl Carbonate (IO_2)$_2$[CO_3], Hosting I^{5+}-Cations. *JACS Au* **2025**, *5*, 4675–4680, DOI: 10.1021/jacsau.5c00829

(6) Bayarjargal, L.; Fruhner, C.-J.; Schrodt, N.; Winkler, B. $CaCO_3$ phase diagram studied with Raman spectroscopy at pressures up to 50 GPa and high temperatures and DFT modeling. *Phys. Earth Planet. Inter.* **2018**, *281*, 31–45, DOI: 10.1016/j.pepi.2018.05.002

(7) Benedetti, L. R.; Loubeyre, P. Temperature gradients, wavelength-dependent emissivity, and accuracy of high and very-high temperatures measured in the laser-heated diamond cell. *High Press. Res.* **2004**, *24*, 423–455, DOI: 10.1080/08957950412331331718

(8) Du, Z.; Amulele, G.; Benedetti, L. R.; Lee, K. K. M. Mapping temperatures and temperature gradients during flash heating in a diamond-anvil cell. *Rev. Sci. Instrum.* **2013**, *84*, 075111, DOI: 10.1063/1.4813704

(9) Wojdyr, M. *Fityk*: a general-purpose peak fitting program. *J. Appl. Cryst.* **2010**, *43*, 1126–1128, DOI: 10.1107/S0021889810030499

(10) Wright, J.; and Giacobbe, C.; and Majku, M. New opportunities at the Materials Science Beamline at ESRF to exploit high energy nano-focus X-ray beams. *Curr. Opin. Solid. St. M.* **2020**, *24*, 100818, DOI: 10.1016/j.cossms.2020.100818

(11) Prescher, C.; Prakapenka, V. B. *DIOPTAS*: a program for reduction of two-dimensional X-ray diffraction data and data exploration. *High. Press. Res.* **2015**, *35*, 223–230, DOI: 10.1080/08957959.2015.1059835

(12) Agilent, CrysAlis PRO, Yarnton, England, **2014**

(13) Aslandukov, A.; Aslandukov, M.; Dubrovinskaia, N.; Dubrovinsky, L. *Domain Auto Finder* (*DAFi*) program: the analysis of single-crystal X-ray diffraction data from polycrystalline sample. *J. Appl. Cryst.* **2022**, *55*, 1383–1391, DOI: 10.1107/S1600576722008081

(14) Dolomanov, O. V.; Bourhis, L. J.; Gildea, R. J.; Howard, J. A. K.; Puschmann, H. *OLEX2*: a complete structure solution, refinement and analysis program. *J. Appl. Cryst.* **2009**, *42*, 339–341, DOI: 10.1107/S0021889808042726

(15) Sheldrick, G. M. *SHELXT* — Integrated space-group and crystal-structure determination. *Acta. Cryst.* **2015**, *A71*, 3–8, DOI: 10.1107/S2053273314026370

(16) Sheldrick, G. M. Crystal structure refinement with *SHELXL*. *Acta. Cryst.* **2015**, *C71*, 3–8, DOI: 10.1107/S2053229614024218

(17) Hohenberg, P.; Kohn, W. Inhomogeneous Electron Gas. *Phys. Rev.* **1967**, *136*, B864–B871, DOI: 10.1103/PhysRev.136.B864

(18) Perdew, J. P.; Burke, K.; Ernzerhof, M. Generalized Gradient Approximation Made Simple. *Phys. Rev. Lett.* **1996**, *77*, 3865–3868, DOI: 10.1103/PhysRevLett.77.3865

(19) Clark, S. J.; Segall, M. D.; Pickard, C. J.; Hasnip, P. J.; Probert, M. I. J.; Refson, K.; Payne, M. C. First principles methods using CASTEP. *Z. Kristallogr.* **2005**, *220*, 567–570, DOI: 10.1524/zkri.220.5.567.65075

(20) Lejaeghere, K.; Bihlmayer, G.; Björkman, T.; Blaha, P.; Blügel, S.; Blum, V.; Caliste, D.; Castelli, I. E.; Clark, S. J.; Dal Corso, A. et al. Reproducibility in density functional theory calculations of solids. *Science* **2016**, *351*, aad3000, DOI: 10.1126/science.aad3000

(21) Tkatchenko, A.; Scheffler, M. Accurate Molecular Van Der Waals Interactions from Ground-State Electron Density and Free-Atom Reference Data. *Phys. Rev. Lett.* **2009**, *102*, 073005, DOI: 10.1103/PhysRevLett.102.073005

(22) Monkhorst, H. J.; Pack, J. D. Special points for Brillouin-zone integrations. *Phys. Rev. B* **1976**, *13*, 5188–5192, DOI: 10.1103/PhysRevB.13.5188

(23) Baroni, S.; de Gironcoli, S.; Dal Corso, A.; Giannozzi, P. Phonons and related crystal properties from density-functional perturbation theory. *Rev. Mod. Phys.* **2001**, *73*, 515–562, DOI: 10.1103/RevModPhys.73.515

(24) Refson, K.; Tulip, P. R.; Clark, S. J. Variational density-functional perturbation theory for dielectrics and lattice dynamics. *Phys. Rev. B* **2006**, *73*, 155114, DOI: 10.1103/PhysRevB.73.155114

(25) Miwa, K. Prediction of Raman spectra with ultrasoft pseudopotentials. *Phys. Rev. B* **2011**, *84*, 094304, DOI: 10.1103/PhysRevB.84.094304

(26) Spek, A. L. Single-crystal structure validation with the program *PLATON*. *J. Appl. Cryst.* **2003**, *36*, 7–13, DOI: 10.1107/S0021889802022112

(27) Dong, H.; Oganov, A. R.; Brazhkin, V. V.; Wang, Q.; Zhang, J.; Esfahani, M. M. D.; Zhou, X.-F.; Wu, F.; Zhu, Q. Boron oxides under pressure: Prediction of the hardest oxides. *Phys. Rev. B* **2018**, *98*, 174109, DOI: 10.1103/PhysRevB.98.174109

(28) Murnaghan, F. The Compressibility of Media under Extreme Pressures. *Proc. Natl. Acad. Sci.* **1944**, *30*, 244–247, DOI: 10.1073/pnas.30.9.244

(29) Birch, F. Finite Elastic Strain of Cubic Crystals. *Phys. Rev.* **1947**, *71*, 809–824, DOI: 10.1103/PhysRev.71.809

(30) Gonzalez-Platas, J.; Alvaro, M.; Nestola, F.; Angel, R. *EosFit7-GUI*: a new graphical user interface for equation of state calculations, analyses and teaching. *J. Appl. Cryst.* **2016**, *49*, 1377–1382, DOI: 10.1107/S1600576716008050